

Understanding the Mass, Momentum and Energy Transfer in the Frozen Soil with Three Levels of Model Complexities

Lianyu Yu¹, Yijian Zeng¹, Zhongbo Su^{1,2}

¹Faculty of Geo-information and Earth Observation (ITC), University of Twente, Enschede, The Netherlands

²Key Laboratory of Subsurface Hydrology and Ecological Effect in Arid Region of Ministry of Education, School of Water and Environment, Chang'an University, Xi'an, China

Correspondence to: Yijian Zeng (y.zeng@utwente.nl); Zhongbo Su (z.su@utwente.nl)

Abstract

10 Frozen ground covers a vast area of Earth surface and has its important ecohydrological implications for cold regions under changing climate. However, it is challenging to characterize the simultaneous transfer of mass and energy in frozen soils. Within the modeling framework of STEMMUS (Simultaneous Transfer of Mass, Momentum and Energy in Unsaturated Soil), the complexity of soil heat and mass transfer model varies from the basic coupled (termed as BCM), to the advance coupled heat and mass transfer (ACM), and further to the
15 explicit consideration of airflow (ACM-AIR). The impact of different model complexities on understanding the mass, momentum and energy transfer in frozen soil was investigated. The model performance in simulating water and heat transfer and surface latent heat flux was evaluated over a typical Tibetan Plateau meadow site. Results indicate that the ACM considerably improved the simulation of soil moisture, temperature and latent heat flux. The analyses of heat budget reveal that the improvement of soil temperature
20 simulations by ACM is attributed to its physical consideration of vapor flow and thermal effect on water flow, with the former mainly functions above the evaporative front and the latter dominates below the evaporative front. The contribution of airflow-induced water and heat transport (driven by the air pressure gradient) to the total mass and energy fluxes is negligible. Nevertheless, given the explicit consideration of airflow, vapor flow and its effects on heat transfer were enhanced during the freezing-thawing transition period.

25 **1. Introduction**

Frozen soils have been reported with significant changes under climate warming (Cheng and Wu, 2007;Hinzman et al., 2013;Biskaborn et al., 2019;Zhao et al., 2019). Changes in the freezing/thawing process can alter soil hydrothermal regimes and water flow pathways, and thus affect vegetation development (Walvoord and Kurylyk, 2016). Such changes will further considerably affect the spatial pattern, the seasonal
30 to interannual variability and long term trends in land surface water, energy and carbon budgets and then the land surface-atmosphere interactions (Subin et al., 2013;Iijima et al., 2014;Schuur et al., 2015;Walvoord and Kurylyk, 2016). Understanding the soil freeze/thaw processes appears to be the necessary path for a better water resources management and ecosystem protection in cold regions.

When soil experiences the freeze/thaw process, there is a dynamic thermal equilibrium system of ice, liquid
35 water, water vapor and dry air in soil pores. Water and heat flow are tightly coupled in frozen soils. Coupled water and heat physics, describing the concurrent flow of liquid, vapor as well as heat flow, was first proposed by Philip and De Vries (1957) (hereafter termed as PdV57), considering the enhanced vapor transport. The PdV57 theory has been widely applied for a detailed understanding of soil evaporation during the drying process (De Vries, 1958;Milly, 1982;De Vries, 1987;Saito et al., 2006;Novak, 2010). The attempts to
40 simulate the coupled water and heat transport in frozen soils started in 1970s (e.g., Harlan, 1973;Guymon and Luthin, 1974). Since then, numerical tools for simulating one-dimensional frozen soil were gradually developed. Flerchinger and Saxton (1989) developed the SHAW model with the capacity of simulating the coupled water and heat transport process. Hansson et al. (2004) accounted for the phase changes in HYDRUS-1D model and verified its numerical stability with rapidly changing boundary conditions.
45 Considering the two components (water and gas) and three water phases (liquid, vapor, and solid), Painter (2011) developed a fully coupled water and heat transport model MarsFlo. Aiming to efficiently deal with the water phase change between liquid and ice, the enthalpy-based frozen soil model (using enthalpy and total water mass instead of temperature and liquid water content as the prognostic variables) was developed and demonstrated its capability to stably and efficiently simulate soil freeze/thaw process (Li et al., 2010;Bao
50 et al., 2016;Wang et al., 2017). These works together with other modifications, simplifications, generate a hierarchy of frozen soil models, see the detailed review by Li et al. (2010) and Kurylyk and Watanabe (2013).

Air flow has been reported important to the soil water and heat transfer process under certain conditions (Touma and Vauclin, 1986;Prunty and Bell, 2007). Zeng et al. (2011a, b) found that soil evaporation is enhanced after precipitation events by considering air flow and demonstrated that the air pressure induced
55 advective fluxes inject the moisture into the surface soil layers and increase the hydraulic conductivity at the top layer. The diurnal variations of air pressure resulted in the vapor circulation between the atmosphere and the land surface. Wicky and Hauck (2017) reported that the temperature difference between the upper and the lower part of a permafrost talus slope was significant and attributed it to the airflow induced convective heat flux. Yu et al. (2018) analyzed the spatial and temporal dynamics of air pressure induced fluxes and

60 found an interactive effect as the presence of soil ice. The abovementioned studies demonstrate that the explicit consideration of air flow has the potential to affect the soil hydrothermal regime. However, to what extent and under what condition air flow plays significant roles in the subsurface heat budgets has not been detailed.

Current land surface models (hereafter LSMs), however, usually adopted a simplified frozen soil physics
65 with relative coarse vertical discretization (Koren et al., 1999;Viterbo et al., 1999;Niu et al., 2011;Swenson et al., 2012). In their parameterizations, soil water and heat interactions can only be indirectly activated by the phase change processes, the mutual dependence of liquid water, water vapor, ice and dry air in soil pores is absent. This mostly leads to oversimplifications of physical representations of hydrothermal and ecohydrological dynamics in cold regions (Novak, 2010;Su et al., 2013;Wang et al., 2017;Cuntz and Haverd,
70 2018;Grenier et al., 2018;Wang and Yang, 2018;Qi et al., 2019). Specifically, Su et al. (2013) evaluated the European Centre for Medium-Range Weather Forecasts (ECMWF) soil moisture analyses over the Tibetan Plateau, and found that HTESSEL cannot capture phase transitions of soil moisture (i.e., underestimation during frozen period while overestimation during thawing). There are continuous efforts in improving parameterizations and representations of cold region dynamics, including frozen ground (Boone et al.,
75 2000;Luo et al., 2003), vapor diffusion (Karra et al., 2014), thermal diffusion (Bao et al., 2016), coupling water and heat transfer (Wang and Yang, 2018), and three-layer snow physics (Wang et al., 2017;Qi et al., 2019). While to our knowledge, few studies have investigated the role of increasing complexities of soil physical processes (from the basic coupled to the advanced coupled water and heat transfer processes, and then the explicit consideration of air flow) in simulating the thermo-hydrological states in cold regions. How
80 and to what extent the complex mutual dependent physics affects the soil mass and energy transfer in frozen soils? Is it necessary to consider a fully coupled physical process in LSMs? These two questions frame the scope of this work.

In this paper, we incorporated various complexities of soil water and heat transport mechanisms into a common modeling framework (STEMMUS-FT, Simultaneous Transfer of Energy, Momentum and Mass in
85 Unsaturated Soils with Freeze-Thaw). With the aid of in situ measurements collected from a typical Tibetan meadow site, the pros and cons of different model complexities were investigated. Subsurface energy budgets and latent heat flux density analyses were further carried out to illustrate the underlying mechanisms of different coupled soil water-heat physics. Section 2 describes the experimental site and three different complexities of subsurface physics within the STEMMUS framework. The performance of different models
90 is presented in Section 3 together with the subsurface heat budgets and latent heat flux density analyses. Section 4 discusses the effects of considering coupled soil water-heat transfer and air flow in frozen soils. The conclusion is drawn in Section 5.

2. Methodology

2.1 Experimental site

95 Maqu station, equipped with a catchment-scale soil moisture and soil temperature (SMST) monitoring
network and micro-meteorological observing system (Su et al., 2011;Dente et al., 2012;Zeng et al., 2016), is
situated on the north-eastern fringe of the Tibetan Plateau (33°30'–34°15'N, 101°38'–102°45'E). According
to the updated Köppen-Geiger climate classification system, it can be characterized as a cold climate with
dry winter and warm summer (Dwb). The mean annual air temperature is 1.2 °C, and the mean air
100 temperatures of the coldest month (January) and warmest month (July) are about -10.0 °C and 11.7 °C,
respectively. Alpine meadows (e.g., *Cyperaceae* and *Gramineae*), with heights varying from 5 cm to 15 cm
throughout the growing season, are the dominant land cover in this region. In situ soil sampling determined
the soil as a mixture of sandy loam, silt loam and organic soil with a maximum of 18.3 % organic matter for
the upper soil layers (Dente et al., 2012;Zheng et al., 2015a;Zhao et al., 2018).

105 The Maqu SMST monitoring network spans an area of approximately 40 km×80 km with the elevation
ranging from 3200 m to 4200 m a.s.l. SMST profiles are automatically measured by 5TM ECH₂O probes
(METER Group, Inc., USA) installed at the soil depths of 5 cm, 10 cm, 20 cm, 40 cm, and 80 cm. The micro-
meteorological observing system includes a 20 m Planetary Boundary Layer (PBL) tower providing the
meteorological measurements at five heights above ground (i.e., wind speed and direction, air temperature
110 and relative humidity), and an eddy-covariance (EC150, Campbell Scientific, Inc., USA) system installed for
measuring the turbulent sensible, latent heat fluxes and carbon fluxes. Four component down and upwelling
solar and thermal radiation (NR01-L, Campbell Scientific, Inc., USA), and liquid precipitation (T200B,
Geonor, Inc., USA) are also monitored.

2.2 Mass and energy transport in unsaturated soils

115 On the basis of STEMMUS modelling framework, the increasing complexity of vadose zone physics in
frozen soils was implemented as three alternative models (Table 1). Firstly, STEMMUS enabled isothermal
water and heat transfer physics (Eqs. 1 & 2). The 1-D Richards equation is utilized to solve the isothermal
water transport in variably saturated soils. The heat conservation equation took into account the
freezing/thawing process and the latent heat due to water phase change. The effect of soil ice on soil hydraulic
120 and thermal properties was considered. It is termed as basic coupled water and heat transfer model (BCM).

Secondly, the fully coupled water and heat physics, i.e., water vapor flow and thermal effect on water flow,
was explicitly considered in STEMMUS, termed as the advanced coupled model (ACM). For the ACM
physics, the extended version of Richards (1931) equation with modifications made by Milly (1982) was
used as the water conservation equation (Eq. 3). Water flow can be expressed as liquid and vapor fluxes
125 driven by both temperature gradients and matric potential gradients. The heat transport in frozen soils mainly
includes: heat conduction (CHF, $\lambda_{eff} \frac{\partial T}{\partial z}$), convective heat transferred by liquid flux (HFL, $-C_L q_L (T - T_r)$,
 $-C_L S (T - T_r)$), vapor flux (HFV, $-C_V q_V (T - T_r)$), the latent heat of vaporization (LHF, $-q_V L_0$), the latent

heat of freezing/thawing ($-\rho_i\theta_iL_f$) and a source term associated with the exothermic process of wetting of a porous medium (integral heat of wetting) ($-\rho_LW\frac{\partial\theta_L}{\partial t}$). It can be expressed as Eq. 4 (De Vries, 1958;Hansson et al., 2004).

Lastly, STEMMUS expressed the freezing soil porous medium as the mutually dependent system of liquid water, water vapor, ice water, dry air and soil grains, in which other than air flow all other components kept the same as in ACM (termed as ACM-AIR model) (Eqs. 5, 6, &7, Zeng et al., 2011a, b;Zeng and Su, 2013). The effects of air flow on soil water and heat transfer can be two-fold. Firstly, the air flow-induced water and vapor fluxes (q_{La} , q_{Va}) and its corresponding convective heat flow (HF_a, $-q_aC_a(T - T_r)$) were considered. Secondly, the presence of air flow alters the vapor transfer processes, thus can considerably affects the water and heat transfer in an indirect manner.

STEMMUS utilized the adaptive time-step strategy, with maximum time steps ranging from 1s to 1800s (e.g., with 1800s as the time step under stable conditions). The maximum desirable change of soil moisture and soil temperature within one time step was set as $0.02\text{ cm}^3\text{ cm}^{-3}$ and $2\text{ }^\circ\text{C}$, respectively, to prevent too large change in state variables that may cause numerical instabilities. If the changes between two adjacent soil moisture/temperature states are less than the maximum desirable change, STEMMUS continues without changing the length of current time step (e.g., 1800s). Otherwise, STEMMUS will adjust the time step with a deduction factor, which is proportional to the difference between the too large changes and desirable allowed maximum changes of state variables. Within one single time step, the Picard iteration was used to solve the numerical problem, and the numerical convergence criteria is set as 0.001 for both soil matric potential (in cm) and soil temperature (in $^\circ\text{C}$).

To accommodate the specific conditions of a Tibetan meadow, the total depth of the soil column was set as 1.6 m (Figure 1). The vertical soil discretization was designed finer for the upper soil layers (0.1-2.5 cm for 0-40 cm, 27 layers) than that for the lower soil layers (5-20 cm for 40-160 cm, 10 layers). Surface boundary for the water transport was set as the flux-type boundary controlled by the atmospheric forcing (i.e., evaporation, precipitation), while the specific soil temperature was assigned as the surface boundary of the energy conservation equation. The free drainage (zero matric potential gradient) and measured soil temperature were set as the bottom boundary conditions for the water transport and heat transport, respectively. For the air flow, the surface boundary was set as the atmospheric pressure and soil air was allowed to escape from the bottom of the soil column. Surface evapotranspiration was calculated using the Penman-Monteith method. Soil evaporation and transpiration can be separately estimated. The available radiation energy is partitioned into the canopy and soil component via LAI, the canopy minimum surface resistance and soil surface resistance are then utilized to calculate the potential transpiration and soil evaporation. Actual transpiration is calculated as the function of potential transpiration and the root length density-weighted available soil liquid water (which is assumed to be zero if soil temperature falls below $0\text{ }^\circ\text{C}$ (Kroes et al., 2009;Orgogozo et al., 2019)). For our simulation period, grassland stepped into the dormancy period as the soil freezes. The accumulative positive temperature during the thawing period was not enough

165 to break the dormancy of vegetation. The contribution of plant transpiration to the land surface heat flux is negligible during the dormancy period. The effect of soil moisture on the actual soil evaporation is taken into account via the soil surface resistance (Eq. A6). All three aforementioned models adopted the same adaptive time-step strategy and numerical solution, the same soil discretization, soil parameters (shown as Table 2) and boundary conditions. Since all three models employed the same mesh resolutions, parameters and boundary conditions, numerical solution and utilized the adaptive time step strategy. It indicated that the
170 truncation errors due to numerical solution among three models were comparable. The difference among models is mainly restricted to the various representations of soil physical processes (e.g., the inclusion of vapor flow and air flow or not).

3. Results

Given the same atmospheric forcing and the same set of parameters, the performance of models with varying
175 complexities of soil water and heat physics was illustrated in Sect. 3.1, 3.2 & 3.3. Sect. 3.4 & 3.5 further analyzed the variations of heat budgets and subsurface latent heat flux density, illustrating differences in the underlying mechanisms among various models.

3.1 Soil hydrothermal profile simulations

The performance of the model with various soil physics in simulating the soil thermal profile information is
180 illustrated in Figure 2. Both ACM and ACM-AIR well reproduced the time series of the soil temperature at different soil depths except for the 40 cm, which is most probably due to the inappropriate measurements (e.g., improper placement of sensors). However, there are significant discrepancies in soil temperature simulated by the BCM. Compared to the observations, a stronger diurnal behavior of soil temperature in response to the fluctuating atmospheric forcing was found and earlier stepping-in/stepping-out of the frozen
185 period was simulated by the BCM. Such differences enlarged at deeper soil layers with large BIAS and RMSE values (Table 3).

Figure 3 presents the time series of observed and simulated soil liquid water content at five soil layers. During the rapid freezing period, a noticeable overestimation of diurnal fluctuations and early and fast decreasing of soil liquid water content was simulated by BCM. Moreover, stronger diurnal fluctuations and early increase
190 of liquid water content were also found during the thawing period. The early thawing of soil water even led to an unrealistic refreezing process at 80 cm (from 88th to 92nd day after December 2015), which is due to the simulated early warming of soil by BCM (Figure 2). Such discrepancies were significantly ameliorated by ACM and ACM-AIR simulations. Nevertheless, all three models can well capture the diurnal variations and magnitude of liquid water content during the frozen period. Note that there is an observable difference
195 between ACM and ACM-AIR simulated soil liquid water content at shallower soil layers during the thawing process (e.g., Figure 3, 5cm).

3.2 Freezing front propagation

The time series of freezing front propagation derived from the measured and simulated soil temperature was reproduced in Figure 4. Initialized from the soil surface, the freezing front quickly develops downwards till
200 the maximum freezing depth. The thawing process starts from both the top and bottom, mainly driven by the atmospheric heat and bottom soil temperature, respectively. Such characteristics were well captured by both the ACM and ACM-AIR model in terms of freezing rate, maximum freezing depth and surface thawing process, while the BCM tended to present a more fluctuated and rapid freezing front propagation and a deeper maximum freezing depth that is early reached. The effect of atmospheric heat source on soil was
205 overestimated by the BCM as shown by the stronger diurnal early onset of the thawing process.

3.3 Surface Evapotranspiration

The performance of the model with different soil physics in reproducing the latent heat flux dynamics is shown in Figure 5. Compared to the observed LE, there is a significant overestimation of half-hourly latent heat flux, which significantly degraded the overall performance using BCM. The occurrence of such
210 overestimation was notably reduced using ACM and ACM-AIR. The general underestimation of latent heat flux by the ACM and ACM-AIR was found mostly during the freezing-thawing transition period (Figure 6b), when the soil hydrothermal states are not well captured (Figure 2 &3).

The overestimation of surface evapotranspiration by BCM was significant during the initial freezing and transition period (Figure 6a, December & February). During the rapid freezing period (January), BCM
215 presented a good match in the diurnal variation compared to the observations. The monthly average diurnal variations were found to be well captured by ACM and ACM-AIR. Figure 6b shows the comparison of observed and simulated cumulative surface evapotranspiration. The overall overestimation of surface evapotranspiration by BCM can be clearly seen in Figure 6b. Days at the initial freezing periods, with high liquid water content simulations, accounted for more than 90% of the overestimation. The initial stage
220 overestimation of surface evapotranspiration was significantly reduced by ACM and ACM-AIR. Slight underestimation of cumulative surface evapotranspiration was simulated by ACM and ACM-AIR with values of 3.98% and 4.78%, respectively.

3.4 Heat budgets

Figure 7 shows the time series of simulated energy budget components at 5 cm using BCM, ACM and ACM-AIR during the freezing period (5th - 11th day after 1 December) and freezing-thawing transition period (83rd
225 - 89th day after 1 December). For the BCM, only the change rate of heat content HC and conductive heat flux divergence CHF are considered as the LHS and RHS of Eq. 2 (see Table 1). Three additional terms, convective heat flux divergence of liquid flow HFL and vapor flow HFV, and latent heat flux divergence were included for the ACM. While for the ACM-AIR, the convective heat flux divergence of air flow HFa
230 was further added.

There is a strong diurnal variation of heat budget components (HC, CHF & LHF, Table 1), corresponding to the diurnal fluctuation of soil temperature. For the BCM, the change rate of heat content was almost completely balanced by the conductive heat flux divergence CHF (Figure 7a). Compared to the BCM, a stronger diurnal fluctuation of HC and CHF was found in ACM results. Inferred from results in Figure 2, the time series of soil temperature change ($\partial T/\partial t$) simulated by BCM was larger than that simulated by ACM. This indicates BCM produced less fluctuation of apparent heat capacity ($C_{app} = C_{soil} + \rho_i \frac{L_f^2}{gT} \frac{d\theta_L}{d\psi}$) than ACM. During the freezing period, the latent heat flux divergence LHF was lower than conductive heat flux divergence CHF by 1-2 orders of magnitude (Figure 7b). The positive value of LHF term during daytime indicates condensation happens at 5 cm, as water vapor moves downward. The convective heat fluxes of liquid flow and vapor flow were even smaller compared to conductive heat flux (Figure 7b). There is no significant difference of heat budget components between ACM and ACM-AIR in terms of diurnal variation and magnitude. The convective heat flux divergence of air flow played a negligible role in the change of thermal state (HC) (Figure 7c).

The dynamics of heat balance components at 5 cm soil layer was simulated for the freezing-thawing transition period (Figure 7d, e, f). Both HC and CHF underwent strong diurnal variations with increasing fluctuation magnitude, indicating soil warming at 5 cm. For the ACM, CHF outnumbered HC during daytime and the difference increased with time. Negative values were found for LHF and developed further over time. The sum of CHF and LHF nearly balanced the HC term. Such behavior was similarly reproduced by ACM-AIR with a slightly large difference between HC and CHF terms. This means a larger amount of water vapor was evaporated from 5 cm soil layer (with more negative LHF term) from ACM-AIR simulations than that from ACM simulations, which explains the lower liquid water content for ACM-AIR (Figure 3, 5 cm).

3.5 Subsurface latent heat flux density

To give more context to the results, the spatial and temporal distributions of simulated latent heat flux density (S_h), $-\rho_w L \partial q_v / \partial z$, during the freezing and freezing-thawing transition period were shown in Figure 8. For the BCM, the latent heat flux density (S_h) is not available as it neglects the vapor flow.

Figure 8a shows that there is a strong diurnal variation of S_h at upper 0.1 cm soil layers. Such diurnal behavior along the soil profile was interrupted at 1 cm, at which the water vapor consistently moved upwards as evaporation source (termed as evaporative front). The path of this upward water vapor was disrupted at 20 cm from the 6th of December, where the freezing front developed. Compared to the upper 0.1 cm soil, a weaker diurnal fluctuation of S_h was found at lower soil layers. For ACM-AIR, the vapor transfer patterns were similar to that of ACM (Figure 8b). There were isolated connections of condensed water vapor between upper 1 cm soil and the lower soil layers ($S_h > 0$, e.g., 6th, 7th, 9th, and 10th of December), possibly associated with the downward air flow (see Figure 12 in Yu et al. (2018)). The large difference in magnitude of latent heat flux density between ACM and ACM-AIR appeared mainly isolated at upper soil layers (Figure 8c). At soil layers between 1 cm and 20 cm, ACM-AIR simulated less in condensation vapor area ($S_h > 0$) and more

in the evaporation area ($S_n < 0$), indicating that ACM-AIR produced an additional amount of condensation and evaporation water vapor compared with ACM (Figure 8c).

270 Similar to that during the freezing period, the S_n during the transition period can be characterized as: strong diurnal variations at upper soil layers; interruption of diurnal patterns by the constant upward evaporation of intermediate soil layers; and weak diurnal variations at lower soil layers (Figure 8d, e). While the maximum evaporation rate was less than that during the freezing period. The consistent evaporation zone developed to a depth of 5 cm. The path for the upwards water vapor tended to develop deeper than 30 cm with the absence of soil ice. The simulation by ACM-AIR produced more condensation and less evaporative water vapor than that by ACM (Figure 8f). In addition, steadily more evaporative water vapor from 5 cm was simulated by
275 ACM-AIR compared to ACM. This confirms the aforementioned point that during the freezing-thawing transition period, large LHF values were simulated by ACM-AIR (Figure 7).

4. Discussion

4.1 Coupled Water and Heat Transfer Processes

Vapor flow, which is dependent on soil matric potential and temperature, links soil water and heat transfer
280 processes. The mutual dependence of soil water, in different phases (liquid, water vapor, and ice), and heat transport is enabled to facilitate our better understanding of the complex soil physical processes (e.g., Figure 7-8). Specifically, the interdependence of soil moisture and soil temperature (SMST) profiles simulated by ACM was closer to the observation than that by BCM. In addition, significant enhancement in portraying the monthly average diurnal variations of surface evapotranspiration and cumulative evapotranspiration can be
285 found from ACM simulations, which constrains the hydrothermal regimes especially during the freezing-thawing transition periods (Figure 2, 3& 6).

During the freezing period, liquid water in the soil freezes, which is analog to the soil drying process, and water vapor fluxes instead of liquid fluxes dominate the mass transfer process (Zhang et al., 2016). Neglecting such important water flux component unavoidably results in different/unrealistic simulations of surface
290 evapotranspiration and SMST profiles (Li et al., 2010; Karra et al., 2014; Wang and Yang, 2018). Li et al. (2010) reported that vapor fluxes were comparable to the liquid water fluxes and affected the freezing/melting processes. On the basis of long term one-dimensional soil column simulations, Karra et al. (2014) reported that the inclusion of the vapor diffusion effect significantly increased the thickness of the ice layer as explained by the positive vapor cold trapping-thermal conductivity feedback mechanism. From the energy
295 budget perspective, latent heat fluxes contribute more, due to the vapor phase change (LHF), to the heat balance budget at soil layers above the evaporative front than that below it (see LHF in Figure 7e vs. Figure 7b, corresponding evaporative front shown as Figure 8d vs. Figure 8a). This is consistent with findings by Zhang et al. (2016), who presented that the latent heat of vapor due to phase change is two orders of magnitude less than the heat fluxes due to conduction during winter time and corresponds to our results of

300 Figure 7b & c during the freezing period. While our results further showed that the latent heat fluxes due to
vapor phase change can be considerable during the transition period (Figure 7e & f). The downward latent
heat flux from ACM makes the subsurface soil warmer, which reduces the temperature gradient ($\partial T/\partial z$)
(Wang and Yang, 2018). This further results in the weaker diurnal fluctuations of HC term in ACM than that
in BCM (see HC in Figure 7e vs. Figure 7d). At the soil layers below the evaporative front, the heat flux
305 source from the vapor transfer process (LHF) is negligible (e.g., Figure 7b). The thermal retard effect as the
presence of soil ice, expressed as the apparent heat capacity term (C_{app}), dominates the heat transfer process
in frozen soils. By considering the thermal effect on water flow, ACM usually has a larger water capacity
value $\partial\theta/\partial\psi$ than BCM does. As such, the intense thermal impedance effect leads to the results that ACM
produced a weaker diurnal fluctuation of soil temperature than BCM at subsurface soil layers (e.g., Figure 2,
310 20 cm).

4.2 Air Flow in the Soil

Since soil pores are filled with liquid water, vapor and dry air, taking dry air as an independent state variable
can facilitate a better understanding of the relative contribution of each component to the mass and heat
transfer in soils. The results show that the dry air-induced water and heat flow is negligible to the total mass
and energy transfer (Zeng et al., 2011b; Yu et al., 2018). Nevertheless, dry air can affect soil hydrothermal
315 regimes significantly under certain circumstances. Wicky and Hauck (2017) reported that the airflow-induced
convective heat transfer resulted in a considerable temperature difference between the upper and lower part
of a permafrost talus slope and thus had a remarkable effect on the thermal regime of the talus slope. Zeng et
al. (2011b) demonstrated the airflow-induced surface evaporation enhanced after precipitation events, since
320 the hydraulic conductivity of topsoil layers increased tremendously due to the increased topsoil moisture by
the injected airflow from the moist atmosphere. In this study, we found that the explicit consideration of
airflow introduced an additional amount of subsurface condensation and evaporative water vapor in the
condensation region and evaporation region, respectively (Figure 8c & f). The effect of latent heat flux on
heat transfer was enhanced by airflow during the freezing-thawing transition period (Figure 7), which further
325 affected the subsurface hydrothermal simulations (e.g., Figure 3).

5. Conclusions

On the basis of STMMUS modeling framework with various representations of water and heat transfer
physics (BCM, ACM and ACM-AIR), the performance of each model in simulating water and heat transfer
and surface evapotranspiration was evaluated over a typical Tibetan meadow ecosystem,. Results indicated
330 that compared to in situ observations, the BCM tended to present earlier freezing and thawing dates with a
stronger diurnal variation of soil temperature/liquid water in response to the atmospheric forcing. Such
discrepancies were considerably reduced by the model with the advanced coupled water-heat physics.
Surface evapotranspiration was overestimated by BCM, mainly due to the mismatches during the initial
freezing and freezing-thawing transition period. ACM models, with the coupled constraints from the

335 perspective of water and energy conservation, significantly improve the model performance in mimicking
the surface evapotranspiration dynamics during the frozen period. The analysis of heat budget components
and latent heat flux density revealed that the improvement of soil temperature simulations by ACM is
ascribed to its physical consideration of vapor flow and thermal effect on water flow, with the former mainly
functions at regions above the evaporative front, and the latter dominates below the evaporative front. The
340 non-conductive heat processes (liquid/vapor/air induced heat convection flux) contributed very minimal to
the total energy fluxes during the frozen period except the latent heat flux divergence at the topsoil layers.
The contribution of airflow induced water and heat flow to the total mass and energy fluxes is negligible.
However, given the explicit consideration of airflow, the latent heat flux and its effect on heat transfer were
enhanced during the freezing-thawing transition period. This work highlighted the role of considering the
345 vapor flow, thermal effect on water flow, and airflow in portraying the subsurface soil hydrothermal
dynamics, especially during freezing-thawing transition periods. To sum up, this study can contribute to a
better understanding of freeze-thaw mechanisms of frozen soils, which will subsequently contribute to the
quantification of permafrost carbon feedback (Burke et al., 2013;Kevin et al., 2014;Schuur et al., 2015), if
the STEMMUS-FT model is to be coupled with a biogeochemical model, as lately implemented (Yu et al.,
350 2020).

Data availability. The soil hydraulic/thermal property data can be freely downloaded from 4TU. Center for
Research Data (<https://doi.org/10.4121/uuid:61db65b1-b2aa-4ada-b41e-61ef70e57e4a>). Some relevant data
are made available from 4TU. Center for Research Data (<https://doi.org/10.4121/uuid:cc69b7f2-2448-4379-b638-09327012ce9b>).
355

Author contribution. Conceptualization, Z.S. and Y.Z.; methodology, L.Y., Y.Z.; writing - original draft
preparation, L.Y., Y.Z.; writing – review & editing, L.Y., Y.Z., Z.S..

360 *Competing interests.* The authors declare that they have no conflict of interest.

Acknowledgment

This work is supported by the National Natural Science Foundation of China (grant no. 41971033) and
supported by the Fundamental Research Funds for the Central Universities, CHD (grant no. 300102298307).
365 The authors thank the editor and referees very much for their constructive comments on improving the
manuscript.

Appendix

A1. Calculation of surface evapotranspiration

370 The one step calculation of actual soil evaporation (E_s) and potential transpiration (T_p) is achieved by incorporating canopy minimum surface resistance and actual soil resistance into the Penman-Monteith model (i.e., the ET_{dir} method in Yu et al. (2016)). LAI is implicitly used to partition available radiation energy into the radiation reaching the canopy and soil surface.

$$T_p = \frac{\Delta(R_n^c - G) + \rho_a c_p \frac{(e_s - e_a)}{r_a^c}}{\lambda(\Delta + \gamma \left(1 + \frac{r_{c,min}}{r_a^c}\right))} \quad (A1)$$

$$E_s = \frac{\Delta(R_n^s - G) + \rho_a c_p \frac{(e_s - e_a)}{r_a^s}}{\lambda(\Delta + \gamma \left(1 + \frac{r_s}{r_a^s}\right))} \quad (A2)$$

375 where R_n^c and R_n^s ($\text{MJ m}^{-2} \text{ day}^{-1}$) are the net radiation at the canopy surface and soil surface, respectively; ρ_a (kg m^{-3}) is the air density; c_p ($\text{J kg}^{-1} \text{ K}^{-1}$) is the specific heat capacity of air; r_a^c and r_a^s (s m^{-1}) are the aerodynamic resistance for canopy surface and soil surface, respectively; $r_{c,min}$ (s m^{-1}) is the minimum canopy surface resistance; and r_s (s m^{-1}) is the soil surface resistance.

The net radiation reaching the soil surface can be calculated using the Beer's law:

$$R_n^s = R_n \exp(-\tau LAI) \quad (A3)$$

And the net radiation intercepted by the canopy surface is the residual part of total net radiation:

$$R_n^c = R_n(1 - \exp(-\tau LAI)) \quad (A4)$$

380 The minimum canopy surface resistance $r_{c,min}$ is given by:

$$r_{c,min} = r_{l,min}/LAI_{eff} \quad (A5)$$

where $r_{l,min}$ is the minimum leaf stomatal resistance; LAI_{eff} is the effective leaf area index, which considers that generally the upper and sunlit leaves in the canopy actively contribute to the heat and vapor transfer.

The soil surface resistance can be estimated following van de Griend and Owe (1994),

$$\begin{aligned} r_s &= r_{sl} & \theta_1 > \theta_{min}, h_1 > -100000 \text{ cm} \\ r_s &= r_{sl} e^{a(\theta_{min} - \theta_1)} & \theta_1 \leq \theta_{min}, h_1 > -100000 \text{ cm} \\ r_s &= \infty & h_1 \leq -100000 \text{ cm} \end{aligned} \quad (A6)$$

385 where r_{sl} (10 s m^{-1}) is the resistance to molecular diffusion of the water surface; a (0.3565) is the fitted parameter; θ_1 is the topsoil water content; θ_{min} is the minimum water content above which soil is able to deliver vapor at a potential rate.

The root water uptake term described by Feddes et al. (1978) is:

$$S(h) = \alpha(h)S_p \quad (\text{A7})$$

where $\alpha(h)$ (dimensionless) is the reduction coefficient related to soil water potential h ; and S_p (s^{-1}) is the potential water uptake rate.

$$S_p = b(z)T_p \quad (\text{A8})$$

390 where $b(z)$ is the normalized water uptake distribution, which describes the vertical variation of the potential extraction term, S_p , over the root zone. Here the asymptotic function was used to characterize the root distribution as described in (Gale and Grigal, 1987; Jackson et al., 1996; Yang et al., 2009; Zheng et al., 2015b). T_p is the potential transpiration in (A1).

395 **Notation**

Symbol	Parameter	Unit	Value
a	Fitted parameter for soil surface resistance	-	0.3565
$b(z)$	Normalized water uptake distribution	m^{-1}	
C_a	Specific heat capacity of dry air	$J\ kg^{-1}\ ^\circ C^{-1}$	1.005
C_{app}	Apparent heat capacity	$J\ kg^{-1}\ ^\circ C^{-1}$	$= C_{soil} + \rho_i \frac{L_f^2}{gT} \frac{d\theta_L}{d\psi}$
C_i	Specific heat capacity of ice	$J\ kg^{-1}\ ^\circ C^{-1}$	2.0455
C_L	Specific heat capacity of liquid	$J\ kg^{-1}\ ^\circ C^{-1}$	4.186
C_s	Specific heat capacity of soil solids	$J\ kg^{-1}\ ^\circ C^{-1}$	
C_{soil}	Heat capacity of the bulk soil	$J\ kg^{-1}\ ^\circ C^{-1}$	
C_V	Specific heat capacity of water vapor	$J\ kg^{-1}\ ^\circ C^{-1}$	1.87
c_p	Specific heat capacity of air	$J\ kg^{-1}\ K^{-1}$	
D_e	Molecular diffusivity of water vapor in soil	$m^2\ s^{-1}$	
D_{TD}	Transport coefficient for adsorbed liquid flow due to temperature gradient	$kg\ m^{-1}\ s^{-1}\ ^\circ C^{-1}$	
D_{va}	Advective vapor transfer coefficient	s	
D_{vg}	Gas phase longitudinal dispersion coefficient	$m^2\ s^{-1}$	
D_{vh}	Isothermal vapor conductivity	$kg\ m^{-2}\ s^{-1}$	
D_{VT}	Thermal vapor diffusion coefficient	$kg\ m^{-1}\ s^{-1}\ ^\circ C^{-1}$	
h	Soil matric potential	m	
H_c	Henry's constant	-	0.02
K	Hydraulic conductivity	$m\ s^{-1}$	
K_g	Intrinsic air permeability	m^2	
K_{Lh}	Isothermal hydraulic conductivities	$m\ s^{-1}$	
K_{LT}	Thermal hydraulic conductivities	$m^2\ s^{-1}\ ^\circ C^{-1}$	
K_s	Soil saturated hydraulic conductivity	$m\ s^{-1}$	
L_0	Latent heat of vaporization of water at the reference temperature	$J\ kg^{-1}$	
LAI_{eff}	Effective leaf area index	-	
L_f	Latent heat of fusion	$J\ kg^{-1}$	3.34E5
n	Van Genuchten fitting parameters	-	
P_g	Mixed pore-air pressure	Pa	
q	Water flux	$kg\ m^{-2}\ s^{-1}$	
q_a	Dry air flux	$kg\ m^{-2}\ s^{-1}$	
q_L	Soil liquid water fluxes (positive upwards)	$kg\ m^{-2}\ s^{-1}$	
q_{La}	Liquid water flux driven by the gradient of air pressure	$kg\ m^{-2}\ s^{-1}$	
q_{Lh}	Liquid water flux driven by the gradient of matric potential	$kg\ m^{-2}\ s^{-1}$	
q_{LT}	Liquid water flux driven by the gradient of temperature	$kg\ m^{-2}\ s^{-1}$	
q_V	Soil water vapor fluxes (positive upwards)	$kg\ m^{-2}\ s^{-1}$	
q_{Va}	Water vapor flux driven by the gradient of air pressure	$kg\ m^{-2}\ s^{-1}$	
q_{Vh}	Water vapor flux driven by the gradient of matric potential	$kg\ m^{-2}\ s^{-1}$	
q_{VT}	Water vapor flux driven by the gradient of temperature	$kg\ m^{-2}\ s^{-1}$	
r_a^c	Aerodynamic resistance for canopy surface	$s\ m^{-1}$	
r_a^s	Aerodynamic resistance for bare soil	$s\ m^{-1}$	

$r_{c,min}$	Minimum canopy surface resistance	$s\ m^{-1}$	
$r_{l,min}$	Minimum leaf stomatal resistance	$s\ m^{-1}$	
r_s	Soil surface resistance	$s\ m^{-1}$	
r_{sl}	Resistance to molecular diffusion of the water surface	$s\ m^{-1}$	10
R_n	Net radiation	$MJ\ m^{-2}\ day^{-1}$	
R_n^c	Net radiation at the canopy surface	$MJ\ m^{-2}\ day^{-1}$	
R_n^s	Net radiation at the soil surface	$MJ\ m^{-2}\ day^{-1}$	
S	Sink term for transpiration	s^{-1}	
S_a	Degree of saturation of the soil air	-	$=1-S_L$
S_L	Degree of saturation in the soil	-	$=\theta_l/\varepsilon$
S_h	Latent heat flux density	$W\ m^{-3}$	$=-\rho_w L \partial q_v / \partial z$
S_p	Potential water uptake rate	s^{-1}	
t	Time	s	
T	Soil temperature	$^{\circ}C$	
T_p	Potential transpiration	$m\ s^{-1}$	
T_r	Arbitrary reference temperature	$^{\circ}C$	20
W	Differential heat of wetting	$J\ kg^{-1}$	
z	Vertical space coordinate (positive upwards)	m	
α	Air entry value of soil	m^{-1}	
$\alpha(h)$	Reduction coefficient related to soil water potential	-	
ε	Porosity	-	
ψ	Water potential	m	
λ_{eff}	Effective thermal conductivity of the soil	$W\ m^{-1}\ ^{\circ}C^{-1}$	
θ	Volumetric water content	$m^3\ m^{-3}$	
θ_i	Soil ice volumetric water content	$m^3\ m^{-3}$	
θ_L	Soil liquid volumetric water content	$m^3\ m^{-3}$	
θ_V	Soil vapor volumetric water content	$m^3\ m^{-3}$	
θ_s	Volumetric fraction of solids in the soil	$m^3\ m^{-3}$	
θ_a	Volumetric fraction of dry air in the soil	$m^3\ m^{-3}$	$=\theta_V$
θ_{sat}	Saturated soil water content	$m^3\ m^{-3}$	
θ_r	Residual soil water content	$m^3\ m^{-3}$	
θ_1	Topsoil water content	$m^3\ m^{-3}$	
θ_{min}	Minimum water content above which soil is able to deliver vapor at a potential rate	$m^3\ m^{-3}$	
ρ_a	Air density	$kg\ m^{-3}$	
ρ_{da}	Density of dry air	$kg\ m^{-3}$	
ρ_i	Density of ice	$kg\ m^{-3}$	920
ρ_L	Density of soil liquid water	$kg\ m^{-3}$	1000
ρ_s	Density of solids	$kg\ m^{-3}$	
ρ_V	Density of water vapor	$kg\ m^{-3}$	
γ_W	Specific weight of water	$kg\ m^{-2}\ s^{-2}$	
μ_a	Air viscosity	$kg\ m^{-2}\ s^{-1}$	
τ	Light extinction coefficient	-	

Reference

- 400 Bao, H., Koike, T., Yang, K., Wang, L., Shrestha, M., and Lawford, P.: Development of an enthalpy-based frozen soil model and its validation in a cold region in China, *Journal of Geophysical Research: Atmospheres*, 121, 5259-5280, 10.1002/2015jd024451, 2016.
- 405 Biskaborn, B. K., Smith, S. L., Noetzli, J., Matthes, H., Vieira, G., Streletskiy, D. A., Schoeneich, P., Romanovsky, V. E., Lewkowicz, A. G., Abramov, A., Allard, M., Boike, J., Cable, W. L., Christiansen, H. H., Delaloye, R., Diekmann, B., Drozdov, D., Eitzelmueller, B., Grosse, G., Guglielmin, M., Ingeman-Nielsen, T., Isaksen, K., Ishikawa, M., Johansson, M., Johannsson, H., Joo, A., Kaverin, D., Kholodov, A., Konstantinov, P., Kröger, T., Lambiel, C., Lanckman, J.-P., Luo, D., Malkova, G., Meiklejohn, I., Moskalenko, N., Oliva, M., Phillips, M., Ramos, M., Sannel, A. B. K., Sergeev, D., Seybold, C., Skryabin, P., Vasiliev, A., Wu, Q., Yoshikawa, K., Zheleznyak, M., and Lantuit, H.: Permafrost is warming at a global scale, *Nature Communications*, 10, 264, 10.1038/s41467-018-08240-4, 2019.
- 410 Boone, A., Masson, V., Meyers, T., and Noilhan, J.: The Influence of the Inclusion of Soil Freezing on Simulations by a Soil–Vegetation–Atmosphere Transfer Scheme, *J Appl Meteorol*, 39, 1544-1569, 10.1175/1520-0450(2000)039<1544:tiotio>2.0.co;2, 2000.
- 415 Burke, E. J., Jones, C. D., and Koven, C. D.: Estimating the Permafrost-Carbon Climate Response in the CMIP5 Climate Models Using a Simplified Approach, *J Clim*, 26, 4897-4909, 10.1175/jcli-d-12-00550.1, 2013.
- Cheng, G., and Wu, T.: Responses of permafrost to climate change and their environmental significance, Qinghai-Tibet Plateau, *Journal of Geophysical Research: Earth Surface*, 112, 10.1029/2006JF000631, 2007.
- 420 Cuntz, M., and Haverd, V.: Physically Accurate Soil Freeze-Thaw Processes in a Global Land Surface Scheme, *Journal of Advances in Modeling Earth Systems*, 10, 54-77, 10.1002/2017MS001100, 2018.
- De Vries, D. A.: Simultaneous transfer of heat and moisture in porous media, *Eos, Transactions American Geophysical Union*, 39, 909-916, 10.1029/TR039i005p00909, 1958.
- De Vries, D. A.: The theory of heat and moisture transfer in porous media revisited, *International Journal of Heat and Mass Transfer*, 30, 1343-1350, [https://doi.org/10.1016/0017-9310\(87\)90166-9](https://doi.org/10.1016/0017-9310(87)90166-9), 1987.
- 425 Dente, L., Vekerdy, Z., Wen, J., and Su, Z.: Maqu network for validation of satellite-derived soil moisture products, *Int J Appl Earth Obs Geoinf*, 17, 55-65, 10.1016/j.jag.2011.11.004, 2012.
- Feddes, R. A., Kowalik, P. J., and Zaradny, H.: Simulation of field water use and crop yield, Centre for Agricultural Publishing and Documentation, Wageningen, the Netherlands, 189 pp., 1978.
- Flerchinger, G. N., and Saxton, K. E.: Simultaneous heat and water model of a freezing snow-residue-soil system. I. Theory and development, *Transactions of the American Society of Agricultural Engineers*, 32, 565-571, 1989.
- 430 Gale, M. R., and Grigal, D. F.: Vertical root distributions of northern tree species in relation to successional status, *Canadian Journal of Forest Research*, 17, 829-834, 10.1139/x87-131, 1987.
- Grenier, C., Anbergen, H., Bense, V., Chanzy, Q., Coon, E., Collier, N., Costard, F., Ferry, M., Frampton, A., Frederick, J., Gonçalves, J., Holmén, J., Jost, A., Kokh, S., Kurylyk, B., McKenzie, J., Molson, J., Mouche, E., Orgogozo, L., Pannetier, R., Rivière, A., Roux, N., Rühaak, W., Scheidegger, J., Selroos, J. O., Therrien, R., Vidstrand, P., and Voss, C.: Groundwater flow and heat transport for systems undergoing freeze-thaw: Intercomparison of numerical simulators for 2D test cases, *Adv Water Resour*, 114, 196-218, 10.1016/j.advwatres.2018.02.001, 2018.
- 435 Guymon, G. L., and Luthin, J. N.: A coupled heat and moisture transport model for Arctic soils, *Water Resour Res*, 10, 995-1001, 10.1029/WR010i005p00995, 1974.
- Hansson, K., Šimůnek, J., Mizoguchi, M., Lundin, L. C., and van Genuchten, M. T.: Water flow and heat transport in frozen soil: Numerical solution and freeze-thaw applications, *Vadose Zone J*, 3, 693-704, 2004.
- 440 Harlan, R. L.: Analysis of coupled heat-fluid transport in partially frozen soil, *Water Resour Res*, 9, 1314-1323, 10.1029/WR009i005p01314, 1973.
- 445 Hinzman, L. D., Deal, C. J., McGuire, A. D., Mernild, S. H., Polyakov, I. V., and Walsh, J. E.: Trajectory of the Arctic as an integrated system, *Ecological Applications*, 23, 1837-1868, 10.1890/11-1498.1, 2013.
- Iijima, Y., Ohta, T., Kotani, A., Fedorov, A. N., Kodama, Y., and Maximov, T. C.: Sap flow changes in relation to permafrost degradation under increasing precipitation in an eastern Siberian larch forest, *Ecohydrology*, 7, 177-187, 10.1002/eco.1366, 2014.
- 450 Jackson, R. B., Canadell, J., Ehleringer, J. R., Mooney, H. A., Sala, O. E., and Schulze, E. D.: A Global

- Analysis of Root Distributions for Terrestrial Biomes, *Oecologia*, 108, 389-411, 1996.
- Karra, S., Painter, S. L., and Lichtner, P. C.: Three-phase numerical model for subsurface hydrology in permafrost-affected regions (PFLOTRAN-ICE v1.0), *Cryosphere*, 8, 1935-1950, 10.5194/tc-8-1935-2014, 2014.
- 455 Kevin, S., Hugues, L., Vladimir, E. R., Edward, A. G. S., and Ronald, W.: The impact of the permafrost carbon feedback on global climate, *Environmental Research Letters*, 9, 085003, 2014.
- Koren, V., Schaake, J., Mitchell, K., Duan, Q. Y., Chen, F., and Baker, J. M.: A parameterization of snowpack and frozen ground intended for NCEP weather and climate models, *Journal of Geophysical Research Atmospheres*, 104, 19569-19585, 1999.
- 460 Kroes, J., Van Dam, J., Groenendijk, P., Hendriks, R., and Jacobs, C.: SWAP version 3.2. Theory description and user manual, Alterra, 2009.
- Kurylyk, B. L., and Watanabe, K.: The mathematical representation of freezing and thawing processes in variably-saturated, non-deformable soils, *Adv Water Resour*, 60, 160-177, 10.1016/j.advwatres.2013.07.016, 2013.
- 465 Li, Q., Sun, S., and Xue, Y.: Analyses and development of a hierarchy of frozen soil models for cold region study, *Journal of Geophysical Research Atmospheres*, 115, 10.1029/2009JD012530, 2010.
- Luo, L., Robock, A., Vinnikov, K. Y., Schlosser, C. A., Slater, A. G., Boone, A., Braden, H., Cox, P., de Rosnay, P., Dickinson, R. E., Dai, Y., Duan, Q., Etchevers, P., Henderson-Sellers, A., Gedney, N., Gusev, Y. M., Habets, F., Kim, J., Kowalczyk, E., Mitchell, K., Nasonova, O. N., Noilhan, J., Pitman, A. J., Schaake, J., Shmakin, A. B., Smirnova, T. G., Wetzell, P., Xue, Y., Yang, Z. L., and Zeng, Q. C.: Effects of frozen soil on soil temperature, spring infiltration, and runoff: Results from the PILPS 2(d) experiment at Valdai, Russia, *J Hydrometeorol*, 4, 334-351, 10.1175/1525-7541(2003)4<334:EOFSOS>2.0.CO;2, 2003.
- 470 Milly, P. C. D.: Moisture and heat transport in hysteretic, inhomogeneous porous media: A matric head-based formulation and a numerical model, *Water Resour Res*, 18, 489-498, 10.1029/WR018i003p00489, 1982.
- 475 Niu, G. Y., Yang, Z. L., Mitchell, K. E., Chen, F., Ek, M. B., Barlage, M., Kumar, A., Manning, K., Niyogi, D., and Rosero, E.: The community Noah land surface model with multiparameterization options (Noah-MP): 1. Model description and evaluation with local-scale measurements, *Journal of Geophysical Research: Atmospheres*, 116, 2011.
- Novak, M. D.: Dynamics of the near-surface evaporation zone and corresponding effects on the surface energy balance of a drying bare soil, *Agr Forest Meteorol*, 150, 1358-1365, <https://doi.org/10.1016/j.agrformet.2010.06.005>, 2010.
- 480 Orgogozo, L., Prokushkin, A. S., Pokrovsky, O. S., Grenier, C., Quintard, M., Viers, J., and Audry, S.: Water and energy transfer modeling in a permafrost-dominated, forested catchment of Central Siberia: The key role of rooting depth, *Permafr Periglac Proc*, 30, 75-89, 10.1002/ppp.1995, 2019.
- 485 Painter, S. L.: Three-phase numerical model of water migration in partially frozen geological media: Model formulation, validation, and applications, *Comput Geosci*, 15, 69-85, 10.1007/s10596-010-9197-z, 2011.
- Philip, J. R., and Vries, D. A. D.: Moisture movement in porous materials under temperature gradients, *Eos, Transactions American Geophysical Union*, 38, 222-232, 10.1029/TR038i002p00222, 1957.
- Prunty, L., and Bell, J.: Infiltration Rate vs. Gas Composition and Pressure in Soil Columns *Soil Sci Soc Am J*, 71, 1473-1475, 10.2136/sssaj2007.0072N, 2007.
- 490 Qi, J., Wang, L., Zhou, J., Song, L., Li, X., and Zeng, T.: Coupled Snow and Frozen Ground Physics Improves Cold Region Hydrological Simulations: An Evaluation at the upper Yangtze River Basin (Tibetan Plateau), *Journal of Geophysical Research: Atmospheres*, 124, 12985-13004, 10.1029/2019jd031622, 2019.
- Richards, L. A.: Capillary Conduction of Liquids Through Porous Mediums, *Physics*, 1, 318, 1931.
- 495 Saito, H., Šimůnek, J., and Mohanty, B. P.: Numerical Analysis of Coupled Water, Vapor, and Heat Transport in the Vadose Zone, *Vadose Zone J*, 5, 784-800, 10.2136/vzj2006.0007, 2006.
- Schuur, E. A. G., McGuire, A. D., Schädel, C., Grosse, G., Harden, J. W., Hayes, D. J., Hugelius, G., Koven, C. D., Kuhry, P., Lawrence, D. M., Natali, S. M., Olefeldt, D., Romanovsky, V. E., Schaefer, K., Turetsky, M. R., Treat, C. C., and Vonk, J. E.: Climate change and the permafrost carbon feedback, *Nature*, 520, 171-179, 10.1038/nature14338, 2015.
- 500 Su, Z., Wen, J., Dente, L., van der Velde, R., Wang, L., Ma, Y., Yang, K., and Hu, Z.: The Tibetan Plateau observatory of plateau scale soil moisture and soil temperature (Tibet-Obs) for quantifying uncertainties in coarse resolution satellite and model products, *Hydrol Earth Syst Sci*, 15, 2303-2316, 10.5194/hess-15-2303-2011, 2011.
- 505 Su, Z., de Rosnay, P., Wen, J., Wang, L., and Zeng, Y.: Evaluation of ECMWF's soil moisture analyses using observations on the Tibetan Plateau, *Journal of Geophysical Research: Atmospheres*, 118, 5304-5318,

- 10.1002/jgrd.50468, 2013.
- Subin, Z. M., Koven, C. D., Riley, W. J., Torn, M. S., Lawrence, D. M., and Swenson, S. C.: Effects of Soil Moisture on the Responses of Soil Temperatures to Climate Change in Cold Regions, *J Clim*, 26, 3139-3158, 10.1175/jcli-d-12-00305.1, 2013.
- 510 Swenson, S. C., Lawrence, D. M., and Lee, H.: Improved simulation of the terrestrial hydrological cycle in permafrost regions by the Community Land Model, *Journal of Advances in Modeling Earth Systems*, 4, 10.1029/2012MS000165, 2012.
- Touma, J., and Vauclin, M.: Experimental and numerical analysis of two-phase infiltration in a partially saturated soil, *Transport in Porous Media*, 1, 27-55, 10.1007/bf01036524, 1986.
- 515 van de Griend, A. A., and Owe, M.: Bare soil surface resistance to evaporation by vapor diffusion under semiarid conditions, *Water Resour Res*, 30, 181-188, 10.1029/93wr02747, 1994.
- Viterbo, P., Beljaars, A., Mahfouf, J. F., and Teixeira, J.: The representation of soil moisture freezing and its impact on the stable boundary layer, *Q J Roy Meteorol Soc*, 125, 2401-2426, 1999.
- 520 Walvoord, M. A., and Kurylyk, B. L.: Hydrologic Impacts of Thawing Permafrost-A Review, *Vadose Zone J*, 15, 10.2136/vzj2016.01.0010, 2016.
- Wang, C., and Yang, K.: A New Scheme for Considering Soil Water-Heat Transport Coupling Based on Community Land Model: Model Description and Preliminary Validation, *Journal of Advances in Modeling Earth Systems*, 10, 927-950, 10.1002/2017ms001148, 2018.
- 525 Wang, L., Zhou, J., Qi, J., Sun, L., Yang, K., Tian, L., Lin, Y., Liu, W., Shrestha, M., Xue, Y., Koike, T., Ma, Y., Li, X., Chen, Y., Chen, D., Piao, S., and Lu, H.: Development of a land surface model with coupled snow and frozen soil physics, *Water Resour Res*, 53, 5085-5103, 10.1002/2017WR020451, 2017.
- Wicky, J., and Hauck, C.: Numerical modelling of convective heat transport by air flow in permafrost talus slopes, *The Cryosphere*, 11, 1311-1325, 10.5194/tc-11-1311-2017, 2017.
- 530 Yang, K., Chen, Y. Y., and Qin, J.: Some practical notes on the land surface modeling in the Tibetan Plateau, *Hydrol Earth Syst Sci*, 13, 687-701, 10.5194/hess-13-687-2009, 2009.
- Yu, L., Zeng, Y., Su, Z., Cai, H., and Zheng, Z.: The effect of different evapotranspiration methods on portraying soil water dynamics and ET partitioning in a semi-arid environment in Northwest China, *Hydrol Earth Syst Sci*, 20, 975-990, 10.5194/hess-20-975-2016, 2016.
- 535 Yu, L., Zeng, Y., Wen, J., and Su, Z.: Liquid-Vapor-Air Flow in the Frozen Soil, *Journal of Geophysical Research: Atmospheres*, 123, 7393-7415, 10.1029/2018jd028502, 2018.
- Yu, L., Zeng, Y., Fatichi, S., and Su, Z.: How vadose zone mass and energy transfer physics affects the ecohydrological dynamics of a Tibetan meadow?, *The Cryosphere Discuss*, 2020, 1-31, 10.5194/tc-2020-88, 2020.
- 540 Zeng, Y., Su, Z., Wan, L., and Wen, J.: Numerical analysis of air-water-heat flow in unsaturated soil: Is it necessary to consider airflow in land surface models?, *Journal of Geophysical Research: Atmospheres*, 116, D20107, 10.1029/2011JD015835, 2011a.
- Zeng, Y., Su, Z., Wan, L., and Wen, J.: A simulation analysis of the advective effect on evaporation using a two-phase heat and mass flow model, *Water Resour Res*, 47, W10529, 10.1029/2011WR010701, 2011b.
- 545 Zeng, Y., Su, Z., van der Velde, R., Wang, L., Xu, K., Wang, X., and Wen, J.: Blending Satellite Observed, Model Simulated, and in Situ Measured Soil Moisture over Tibetan Plateau, *Remote Sensing*, 8, 268, 2016.
- Zeng, Y. J., and Su, Z. B.: *STEMMUS : Simultaneous Transfer of Energy, Mass and Momentum in Unsaturated Soil*, ISBN: 978-90-6164-351-7, University of Twente, Faculty of Geo-Information and Earth Observation (ITC), Enschede, 2013.
- 550 Zhang, M., Wen, Z., Xue, K., Chen, L., and Li, D.: A coupled model for liquid water, water vapor and heat transport of saturated-unsaturated soil in cold regions: model formulation and verification, *Environmental Earth Sciences*, 75, 10.1007/s12665-016-5499-3, 2016.
- Zhao, H., Zeng, Y., Lv, S., and Su, Z.: Analysis of Soil Hydraulic and Thermal Properties for Land Surface Modelling over the Tibetan Plateau, *Earth Syst Sci Data Discuss*, 2018, 1-40, 10.5194/essd-2017-122, 2018.
- 555 Zhao, L., Hu, G., Zou, D., Wu, X., Ma, L., Sun, Z., Yuan, L., Zhou, H., and Liu, S.: Permafrost Changes and Its Effects on Hydrological Processes on Qinghai-Tibet Plateau, *Bulletin of Chinese Academy of Sciences*, 34, 1233-1246, 2019.
- Zheng, D., Van der Velde, R., Su, Z., Wang, X., Wen, J., Booij, M. J., Hoekstra, A. Y., and Chen, Y.: Augmentations to the Noah Model Physics for Application to the Yellow River Source Area. Part I: Soil Water Flow, *J Hydrometeorol*, 16, 2659-2676, 10.1175/JHM-D-14-0198.1, 2015a.
- 560 Zheng, D., Van der Velde, R., Su, Z., Wen, J., Booij, M. J., Hoekstra, A. Y., and Wang, X.: Under-canopy turbulence and root water uptake of a Tibetan meadow ecosystem modeled by Noah-MP, *Water Resour Res*,

51, 5735-5755, 10.1002/2015wr017115, 2015b.

Tables and Figures

565

Table 1. Governing equations for different complexity of water and heat coupling physics (See appendix for notations)

Models	Governing equations (water, heat and air)	Number
BCM	$\frac{\partial \theta}{\partial t} = -\frac{\partial q}{\partial z} - S = \rho_L \frac{\partial}{\partial z} \left[K \left(\frac{\partial \psi}{\partial z} + 1 \right) \right] - S$	(1)
	$\underbrace{C_{soil} \frac{\partial T}{\partial t}}_{HC} - \rho_i L_f \frac{\partial \theta_i}{\partial t} = \frac{\partial}{\partial z} \left(\underbrace{\lambda_{eff} \frac{\partial T}{\partial z}}_{CHF} \right)$	(2)
ACM	$\begin{aligned} \frac{\partial}{\partial t} (\rho_L \theta_L + \rho_V \theta_V + \rho_i \theta_i) &= -\frac{\partial}{\partial z} (q_L + q_V) - S \\ &= -\frac{\partial}{\partial z} (q_{Lh} + q_{LT} + q_{Vh} + q_{VT}) - S \\ &= \rho_L \frac{\partial}{\partial z} \left[K_{Lh} \left(\frac{\partial \psi}{\partial z} + 1 \right) + K_{LT} \frac{\partial T}{\partial z} \right] + \frac{\partial}{\partial z} \left[D_{Vh} \frac{\partial \psi}{\partial z} + D_{VT} \frac{\partial T}{\partial z} \right] - S \end{aligned}$	(3)
	$\begin{aligned} \frac{\partial}{\partial t} \left[\underbrace{(\rho_s \theta_s C_s + \rho_L \theta_L C_L + \rho_V \theta_V C_V + \rho_i \theta_i C_i)(T - T_r) + \rho_V \theta_V L_0 - \rho_i \theta_i L_f}_{HC} \right] - \rho_L W \frac{\partial \theta_L}{\partial t} \\ = \frac{\partial}{\partial z} \left(\underbrace{\lambda_{eff} \frac{\partial T}{\partial z}}_{CHF} \right) - \frac{\partial}{\partial z} \left[\underbrace{q_V L_0}_{LHF} + \underbrace{q_V C_V (T - T_r)}_{HFV} \right] - \frac{\partial}{\partial z} \left[\underbrace{q_L C_L (T - T_r)}_{HFL} \right] - \underbrace{C_L S (T - T_r)}_{HFL} \end{aligned}$	(4)
ACM-AIR	$\begin{aligned} \frac{\partial}{\partial t} (\rho_L \theta_L + \rho_V \theta_V + \rho_i \theta_{ice}) &= -\frac{\partial}{\partial z} (q_{Lh} + q_{LT} + q_{La} + q_{Vh} + q_{VT} + q_{Va}) - S \\ &= \rho_L \frac{\partial}{\partial z} \left[K \left(\frac{\partial \psi}{\partial z} + 1 \right) + D_{TD} \frac{\partial T}{\partial z} + \frac{K}{\gamma_w} \frac{\partial P_g}{\partial z} \right] + \frac{\partial}{\partial z} \left[D_{Vh} \frac{\partial \psi}{\partial z} + D_{VT} \frac{\partial T}{\partial z} + D_{Va} \frac{\partial P_g}{\partial z} \right] - S \end{aligned}$	(5)
	$\begin{aligned} \frac{\partial}{\partial t} \left[\underbrace{(\rho_s \theta_s C_s + \rho_L \theta_L C_L + \rho_V \theta_V C_V + \rho_{da} \theta_a C_a + \rho_i \theta_i C_i)(T - T_r) + \rho_V \theta_V L_0 - \rho_i \theta_i L_f}_{HC} \right] - \rho_L W \frac{\partial \theta_L}{\partial t} \\ = \frac{\partial}{\partial z} \left(\underbrace{\lambda_{eff} \frac{\partial T}{\partial z}}_{CHF} \right) - \frac{\partial}{\partial z} \left[\underbrace{q_V L_0}_{LHF} + \underbrace{q_V C_V (T - T_r)}_{HFV} + \underbrace{q_a C_a (T - T_r)}_{HF_a} \right] \\ - \frac{\partial}{\partial z} \left[\underbrace{q_L C_L (T - T_r)}_{HFL} \right] - \underbrace{C_L S (T - T_r)}_{HFL} \end{aligned}$	(6)
	$\frac{\partial}{\partial t} [\varepsilon \rho_{da} (S_a + H_c S_L)] = \frac{\partial}{\partial z} \left[D_e \frac{\partial \rho_{da}}{\partial z} + \rho_{da} \frac{S_a K_g}{\mu_a} \frac{\partial P_g}{\partial z} - H_c \rho_{da} \frac{q_L}{\rho_L} + (\theta_a D_{Vg}) \frac{\partial \rho_{da}}{\partial z} \right]$	(7)

Table 2. The adopted average values of soil texture and hydraulic properties at different depths (See appendix for notations)

Soil depth (cm)	Clay (%)	Sand (%)	K_s (10^{-6} m s $^{-1}$)	θ_{sat} ($m^3 m^{-3}$)	θ_t ($m^3 m^{-3}$)	α (m^{-1})	n
5-10	9.00	44.13	1.45	0.50	0.035	0.041	1.332
10-40	10.12	44.27	0.94	0.45	0.039	0.041	1.362
40-160	5.59	65.55	0.68	0.41	0.045	0.075	1.590

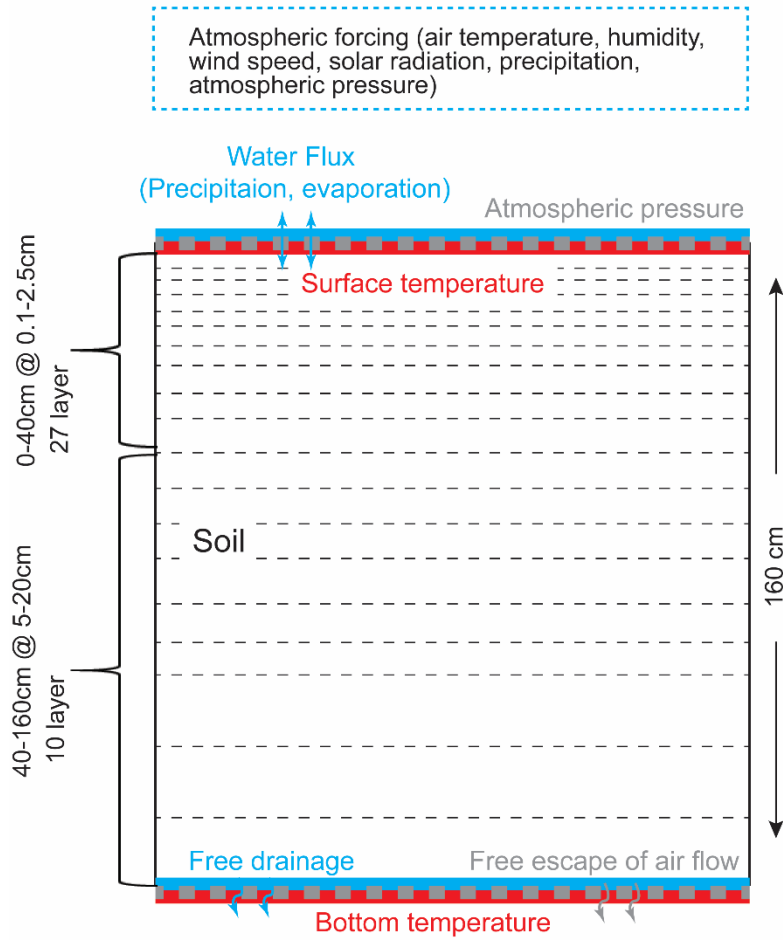
570

Table 3. Comparative statistics values of observed and simulated soil temperature/moisture with three models, with the bold fonts indicating the best statistical performance

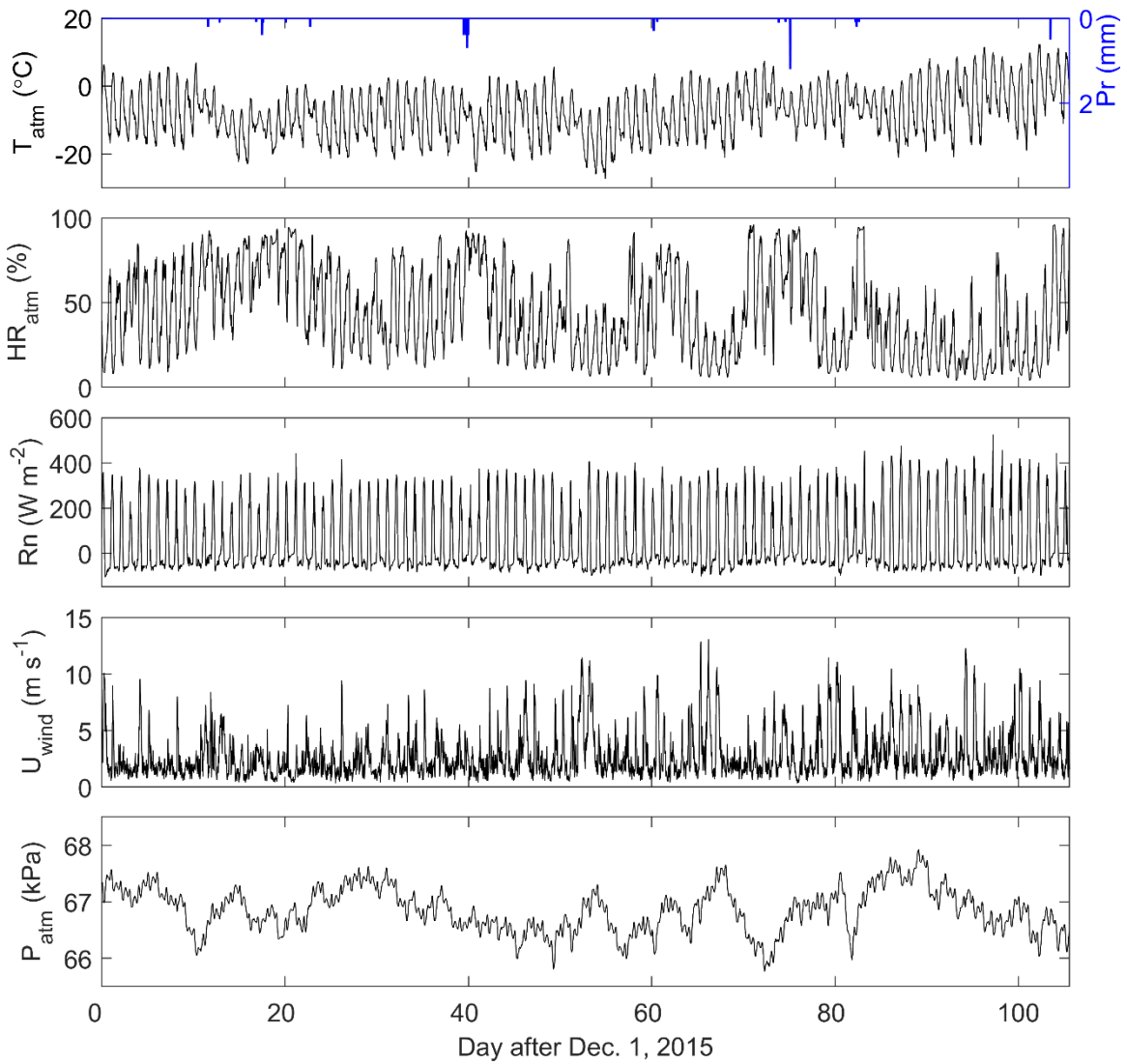
Experiment	Statistics	Soil temperature ($^{\circ}C$)					Soil moisture ($m^3 m^{-3}$)				
		5cm	10cm	20cm	40cm	80cm	5cm	10cm	20cm	40cm	80cm
BCM	BIAS	-0.039	0.177	-0.022	-1.103	-0.140	0.009	0.009	0.005	0.004	0.002
	RMSE	0.381	0.407	0.521	1.524	0.526	0.025	0.022	0.031	0.032	0.012
ACM	BIAS	-0.183	0.093	0.001	-0.956	0.027	0.000	0.004	0.001	0.005	0.001
	RMSE	0.365	0.314	0.186	1.168	0.128	0.008	0.007	0.003	0.007	0.002
ACM-AIR	BIAS	-0.187	0.093	0.005	-0.953	0.029	-0.001	0.004	0.001	0.005	0.001
	RMSE	0.362	0.316	0.180	1.168	0.126	0.011	0.006	0.003	0.007	0.002

575 Note: $BIAS = \frac{\sum_{i=1}^n (y_i - \hat{y}_i)}{n}$, $RMSE = \sqrt{\frac{\sum_{i=1}^n (y_i - \hat{y}_i)^2}{n}}$, where y_i , \hat{y}_i are the measured and model simulated soil temperature/moisture; n is the number of data points.

(a) Model setup

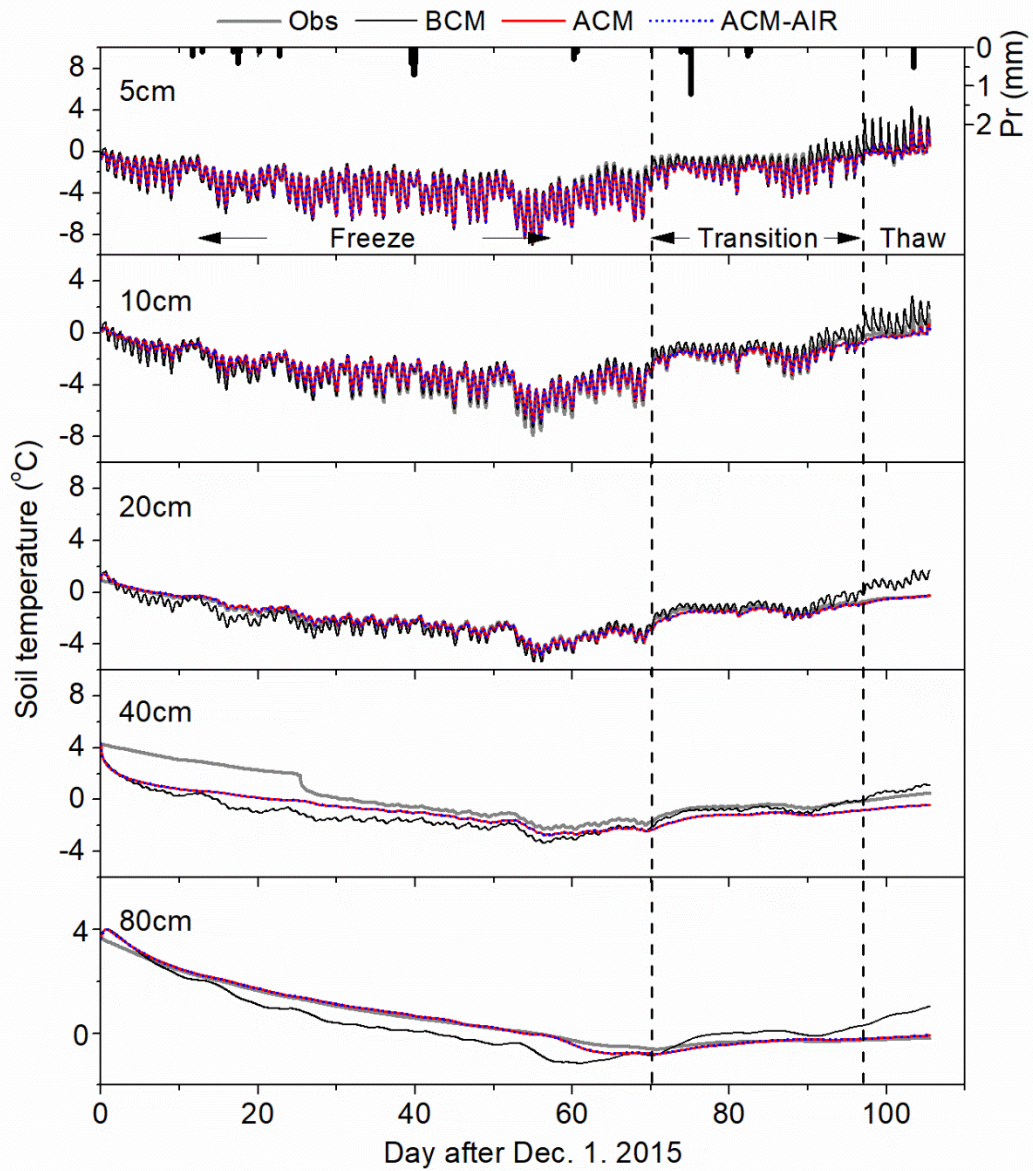


(b) Meteorological Forcing



580

Figure 1. (a) Conceptual illustration of the model setup, the surface/bottom boundary conditions, driving forces, and vertical discretization. (b) Half-hourly measurements of meteorological forcing, including air temperature (T_{atm} , °C), relative humidity (HR_{atm} , %), net radiation (R_n , W m^{-2}), wind speed (U_{wind} , m s^{-1}), and atmospheric pressure (P_{atm} , kPa), during the simulation period. Note that dimensions are not draw to scale, models were ran at one-dimensional scale.



585

Figure 2. Comparison of measured (Obs) and estimated time series of soil temperature at various soil layers using Basic Coupled Model (BCM), Advanced Coupled Model (ACM) and Advanced Coupled Model with Air flow (ACM-AIR).

590

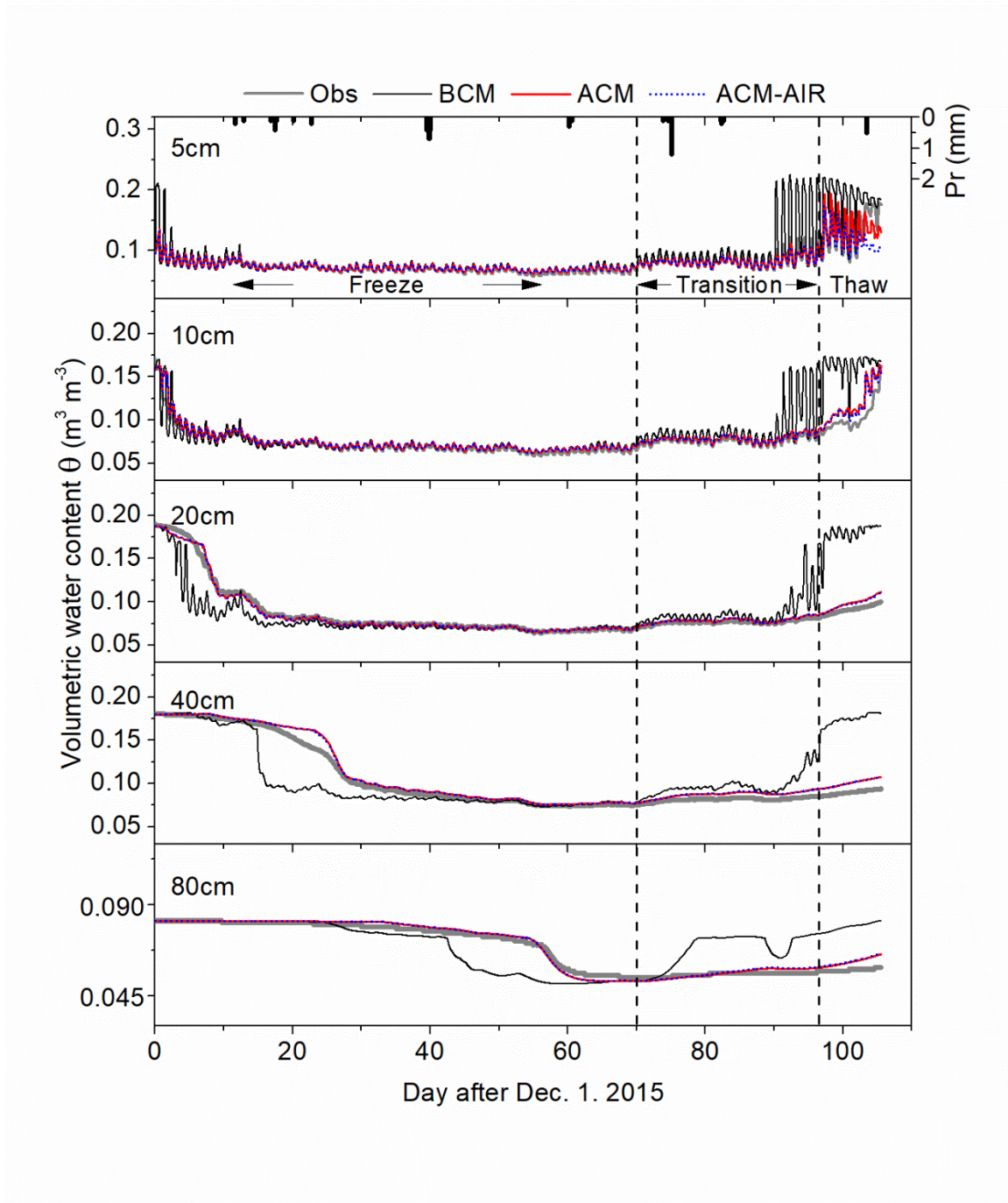
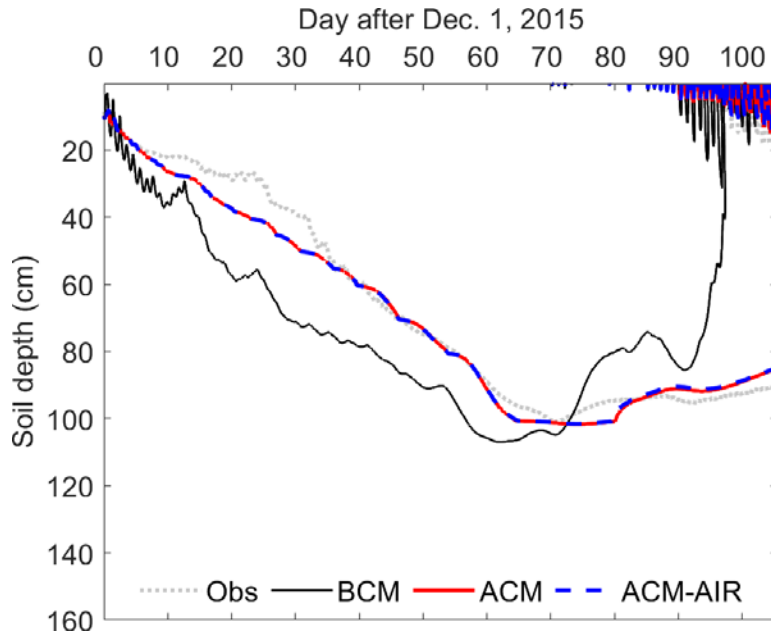
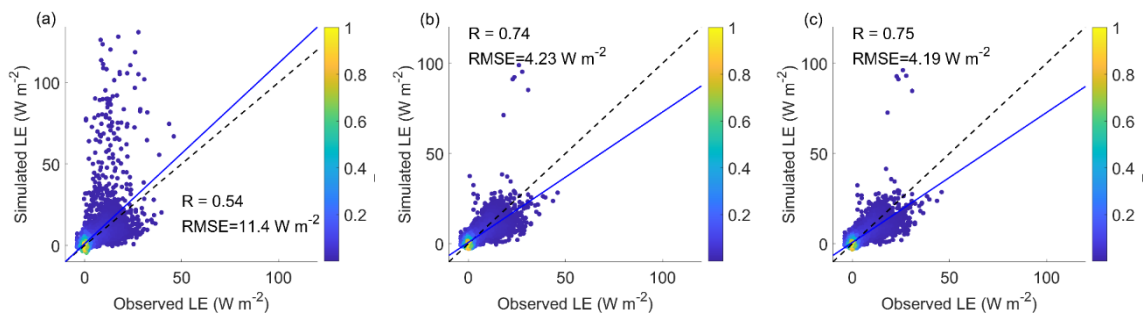


Figure 3. Comparison of measured (Obs) and model simulated time series of soil moisture at various soil layers using Basic Coupled Model (BCM), Advanced Coupled Model (ACM) and Advanced Coupled Model with Air flow (ACM-AIR).



595

Figure 4. Comparison of measured (Obs) and model simulated freezing front propagation (FFP) using Basic Coupled Model (BCM), Advanced Coupled Model (ACM) and Advanced Coupled Model with Air flow (ACM-AIR). Note the measured FFP was seen as the development of zero degree isothermal lines from the measured soil temperature field.



600

Figure 5. Scatter plot of observed and model estimated half-hourly latent heat flux using (a) Basic Coupled Model (BCM), (b) Advanced Coupled Model (ACM) and (c) Advanced Coupled Model with Air flow (ACM-AIR). The color indicates the data composite of surface latent heat flux.

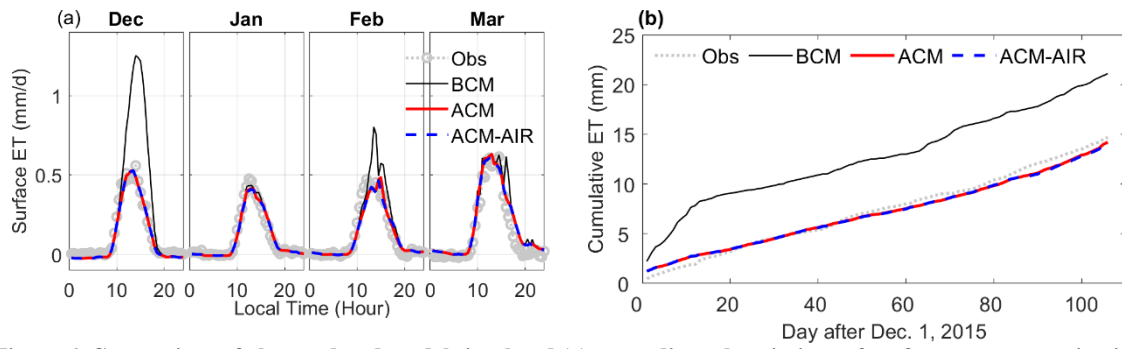
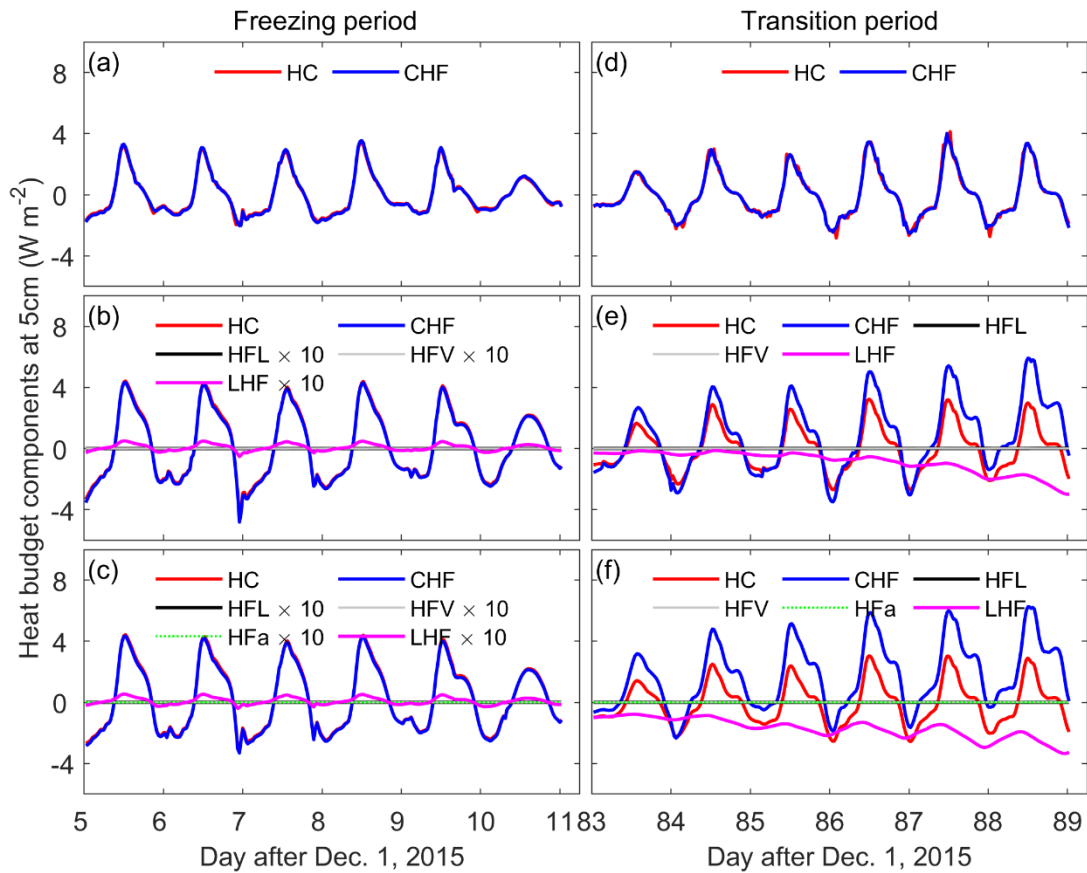


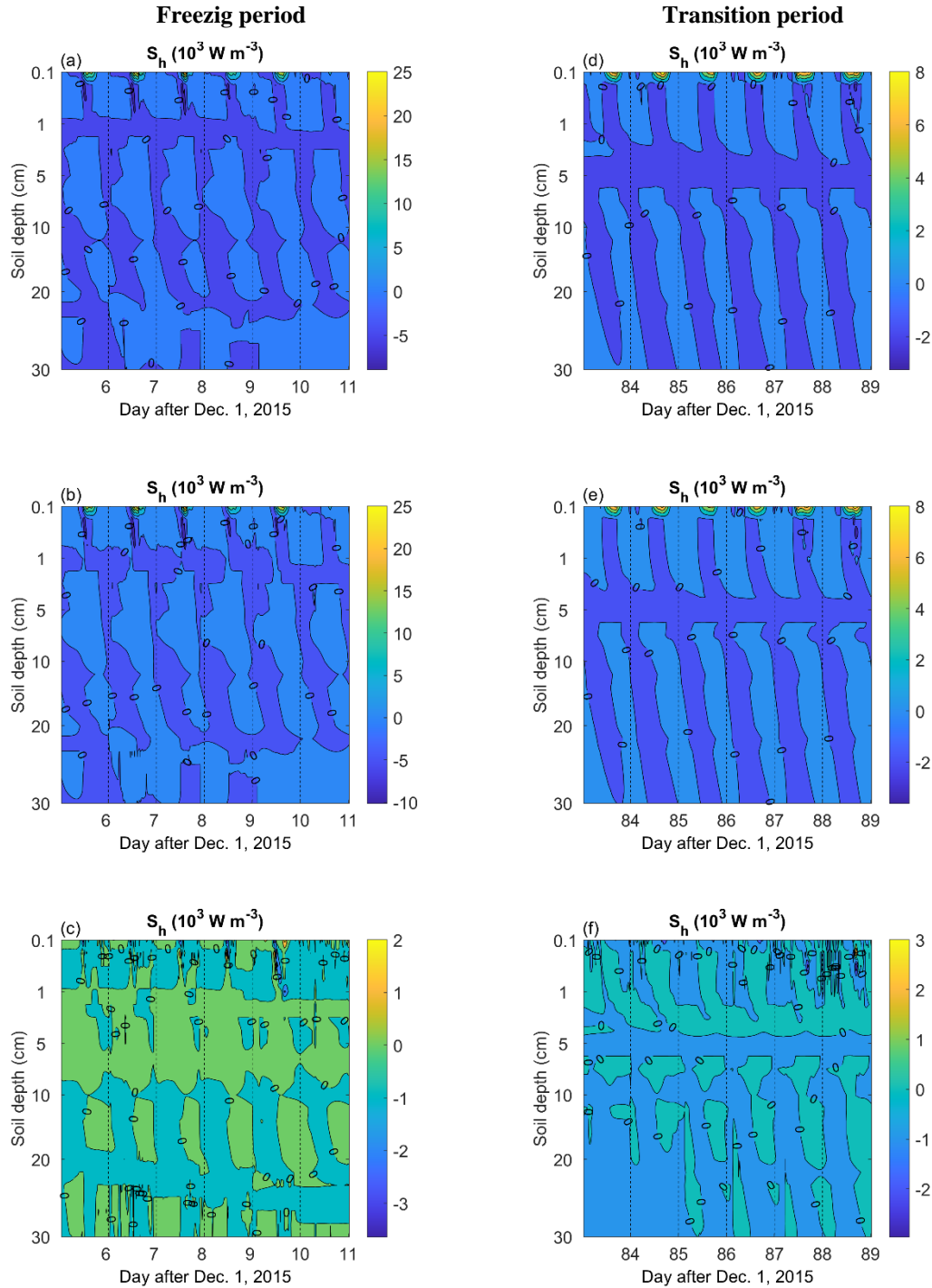
Figure 6. Comparison of observed and model simulated (a) mean diurnal variations of surface evapotranspiration and (b) cumulative evapotranspiration (ET) by Basic Coupled Model (BCM), Advanced Coupled Model (ACM), and Advanced Coupled Model with Air flow (ACM-AIR).

605



610

Figure 7. Time series of model simulated heat budget components at the soil depth of 5cm using (a & d) Basic Coupled Model (BCM), (b & e) Advanced Coupled Model (ACM), and (c & f) Advanced Coupled Model with Air flow (ACM-AIR) simulations during the typical 6-day freezing (left column) and freezing-thawing transition (right column) periods. HC, change rate of heat content, CHF, conductive heat flux divergence, HFL, convective heat flux divergence due to liquid water flow, HFV, convective heat flux divergence due to water vapor flow, HFa, convective heat flux divergence due to air flow, LHF, latent heat flux divergence. Note that for graphical purposes, HFL, HFV, HFa, and LHF were enhanced by a factor of 10 during the freezing period.



615 **Figure 8.** The spatial and temporal distributions of model estimated soil latent heat flux density using (a &d) Advanced Coupled Model (ACM), (b &e) Advanced Coupled Model with Air flow (ACM-AIR) and (c &f) the difference between ACM and ACM-AIR simulations ($S_{h,ACM-AIR} - S_{h,ACM}$) during the typical 6-day freezing and freezing-thawing transition periods. The left and right column are for the freezing and freezing-thawing transition period, respectively. Note that figures for the Basic Coupled Model (BCM) are absent as it can not simulate the subsurface soil latent heat flux density.

620